Published in final edited form as:
Biochemistry. 2008 July 1; 47(26): 6917–6927. doi:10.1021/bi800366d.

Drosophila Frataxin: An Iron Chaperone during Cellular Fe–S Cluster Bioassembly†

Kalyan C. Kondapalli‡, **Nicole M. Kok**‡, **Andrew Dancis**§, and **Timothy L. Stemmler***,‡
Department of Biochemistry and Molecular Biology, Wayne State University, School of Medicine, Detroit, Michigan 48201, and Department of Medicine, Division of Hematology-Oncology, University of Pennsylvania, Philadelphia, Pennsylvania 19104

Abstract

Frataxin, a mitochondrial protein that is directly involved in regulating cellular iron homeostasis, has been suggested to serve as an iron chaperone during cellular Fe–S cluster biosynthesis. In humans, decreased amounts or impaired function of frataxin causes the autosomal recessive neurodegenerative disorder Friedreich's ataxia. Cellular production of Fe–S clusters is accomplished by the Fe cofactor assembly platform enzymes Isu (eukaryotes) and IscU (prokaryotes). In this report, we have characterized the overall stability and iron binding properties of the *Drosophila* frataxin homologue (Dfh). Dfh is highly folded with secondary structural elements consistent with the structurally characterized frataxin orthologs. While the melting temperature ($T_M \approx 59$ °C) and chemical stability ($[\text{urea}]_{50\%} \approx 2.4$ M) of *Drosophila* frataxin, measured using circular dichroism (CD) and fluorescence spectroscopy, closely match values determined for the human ortholog, pure Dfh is more stable against autodegradation than both the human and yeast proteins. The ferrous iron binding affinity ($K_d \approx 6.0\ \mu$M) and optimal metal to protein stoichiometry (1:1) for Dfh have been measured using isothermal titration calorimetry (ITC). Under anaerobic conditions with salt present, holo-Dfh is a stable iron-loaded protein monomer. Frataxin prevents reactive oxygen species-induced oxidative damage to DNA when presented with both Fe(II) and H_2O_2. Ferrous iron bound to Dfh is high-spin and held in a partially symmetric Fe–$(O/N)_6$ coordination environment, as determined by X-ray absorption spectroscopy (XAS). Extended X-ray absorption fine structure (EXAFS) simulations indicate the average Fe–O/N bond length in Dfh is 2.13 Å, consistent with a ligand geometry constructed by water and carboxylate oxygens most likely supplied in part by surface-exposed conserved acidic residues located on helix 1 and strand 1 in the structurally characterized frataxin orthologs. The iron-dependent binding affinity ($K_d \approx 0.21\ \mu$M) and optimal holo-Dfh to Isu monomer stoichiometry (1:1) have also been determined using ITC. Finally, frataxin mediates the delivery of Fe(II) to Isu, promoting Fe–S cluster assembly in vitro. The Dfh-assisted assembly of Fe–S clusters occurs with an observed kinetic rate constant (k_{obs}) of 0.096 min^{-1}.

†This work was supported by the American Heart Association (Grant 0610139Z to K.C.K.) and by the National Institutes of Health (Grant DK068139 to T.L.S. and Grant DK53953 to A.D.).

*To whom correspondence should be addressed: Department of Biochemistry and Molecular Biology, Wayne State University, School of Medicine, 540 E. Canfield Ave., Detroit, MI 48201. Telephone: (313) 577-5712. Fax: (313) 577-2765. E-mail: tstemmle@med.wayne.edu.
‡Wayne State University, School of Medicine.
§University of Pennsylvania.

[1]Abbreviations: NMR, nuclear magnetic resonance; XAS, X-ray absorption spectroscopy; XANES, X-ray absorption near-edge structure; EXAFS, extended X-ray absorption fine structure; ITC, isothermal titration calorimetry; CD, circular dichroism.

SUPPORTING INFORMATION AVAILABLE

CD spectra for folded and unfolded Dfh, characterization of the oligomer states of apo- and holo-Dfh, and Dfh Fe-XANES comparison spectra. This material is available free of charge via the Internet at http://pubs.acs.org.

Frataxin, a nuclear-encoded protein targeted to the mitochondrial matrix in eukaryotes, is essential for the cellular regulation of iron homeostasis (1,2). In humans, a frataxin deficiency is the direct cause of the cardio- and neurodegenerative disorder Friedreich's ataxia (FRDA) (1,3). Cellular phenotypes resulting from frataxin deficiency include disruption in heme and Fe–S cluster cofactor production, mitochondrial iron overload coupled with a reduction in bioavailable metal, and general protein degradation due to an increase in oxidative stress (2, 4,5). In FRDA patients, muscle and nerve cell dysfunction are the most prominent signs of frataxin deficiency (6). Progressive loss of muscle and nerve cell function in patients eventually leads to death typically resulting from complications due to cardiomyopathy.

Although frataxin has been suggested to participate in a variety of different roles associated with cellular iron homeostasis, one essential function for the protein during Fe–S cluster biosynthesis has been firmly established (4,5,7–10). Frataxin can serve as a metallochaperone that delivers ferrous iron to the Fe cofactor assembly scaffold Isu (11). In yeast, [2Fe-2S] cluster assembly is catalyzed by the redundant scaffold proteins Isu1 and Isu2 (12,13). Sulfur from cysteine is supplied by the cysteine desulfurase Nfs1 in association with its essential protein partner Isd11 (14,15). Frataxin's proposed role as a metallochaperone during Fe–S cluster biosynthesis is based in part on the protein's in vitro ability to bind ferrous iron with micromolar binding affinity (11,16–22). In addition, frataxin directly binds Isu in an iron-dependent manner with a submicromolar binding affinity, and its presence stimulates [2Fe-2S] cluster production during activity assays (11). In mitochondrial lysates, yeast frataxin interacts with Isu (and with Nfs1), and in vivo, frataxin depletion is associated with a specific defect in the de novo Fe–S cluster formation on Isu (23,24). The strong sequence conservation of frataxin and Isu orthologs across species indicates a conserved mechanism for Fe(II) delivery and Fe–S cluster production.

The *Drosophila* model has provided additional insight into the role of frataxin directly within a multicellular eukaryotic organism. The frataxin gene in *Drosophila melanogaster* (Dfh) has been identified, and the expressed protein shares a high degree of sequence homology and projected fold with other frataxin orthologs (25). Deficiency of Dfh results in diminished activities of numerous heme- and iron–sulfur cluster-containing enzymes, loss of intracellular iron homeostasis, and increased susceptibility to iron toxicity (26). A direct role in controlling cellular oxidative stress has been shown for frataxin using the *Drosophila* model, with activity directed specifically at aconitase repair and stability (27,28). Interestingly, scavenging cellular hydrogen peroxide through enhanced catalase expression rescues the adverse effects of cellular Dfh deficiency, indicating that H_2O_2 is the important pathogenic substrate underlying FRDA phenotypes in *Drosophila* and that interventions reducing this specific ROS can effectively ameliorate these phenotypes (29). Given the utility of the *Drosophila* model for identifying and characterizing in vivo phenotypes associated with cellular frataxin deficiency and the ability to directly test frataxin's functional role in regulating cellular iron homeostasis and oxidative damage within this multicellular organism, we chose to undertake a thorough characterization of Dfh.

In this report, we provide a comprehensive characterization of the mature Dfh protein's biophysical and metal binding properties and an evaluation of the protein's ability to transfer Fe(II) to Isu during in vitro Fe–S cluster assembly. Thermal and chemical denaturation profiles, obtained using circular dichroism (CD) and fluorescence spectroscopy, provide a basic understanding of the physical characteristics of Dfh. The oligomeric states of apo- and holo-Dfh were characterized using size-exclusion chromatography. The metal binding affinity for apo-Dfh, and the binding affinity of holo-Dfh for Isu, were characterized using isothermal titration calorimetry (ITC). Chemical H_2O_2 degradation assays were performed with holo-Dfh to investigate the protein's ability to inhibit reactive oxygen species production and diminish subsequent oxidative stress to DNA. X-ray absorption spectroscopy (XAS) studies were

performed to clarify the electronic and structural characteristics of Fe(II) bound to Dfh. Finally, in vitro activity assays were used to test Dfh's ability to deliver ferrous iron to Isu and promote Fe–S cluster assembly. These studies further establish frataxin's role as the putative iron chaperone during Fe cofactor production.

MATERIALS AND METHODS

Cloning, Expression, and Protein Purification

Drosophila frataxin cDNA, prepared from the adult testes tissue, was supplied in a pOTB7 vector by the Drosophila Genomics Resource Center (clone AT09528). cDNA was PCR amplified, using the primers 5′-CACCATGAGCAGTCAAATTGAGACGGAA-3′ (5′ extension for TOPO cloning is underlined) and 5′-TTAACTACAGTAGGGCAGGCGT-3′, to subclone full-length frataxin into the directional pET101/D-TOPO expression vector. The sequence represents Dfh residues 59–190 of the complete open reading frame excluding the mitochondrial targeting sequence. Positive clones were verified by DNA sequencing. The recombinant plasmid was transformed into BL21(DE3) *Escherichia coli* competent cells for protein expression.

The expression and stepwise purification of the 133-amino acid Dfh protein (which includes an N-terminal methionine) closely followed our protocol outlined for the yeast frataxin ortholog (21). *E. coli* competent cells were grown at 37 °C. Dfh expression was induced at an OD_{600} of 0.4 with 1 mM IPTG for 5 h, and cells were lysed with a French press and sonicated to liberate protein and disrupt DNA. Pure protein expressed at a mass of 50 mg/L of cell medium. Two ammonium sulfate precipitation steps (40% using the supernatant, 65% using the precipitate) were performed to produce a partially purified Dfh pellet. This pellet was dialyzed twice against a 1:200 volume dilution of buffer A [25 mM Tris-HCl, 10 mM EDTA, and 5 mM β-mercaptoethanol (pH 8)] for at least 6 h. Following dialysis, protein was subjected to anion exchange chromatography using a Q-Sepharose column (Pharmacia) equilibrated in buffer A and eluted using a sodium chloride salt gradient (also in buffer A) up to a final concentration of 1 M. Dfh eluted at a sodium chloride concentration of 500 mM. Following two additional dialysis steps, the protein was subjected to a Phenyl-Sepharose column (Pharmacia) run using buffer A and a reverse 1 M ammonium sulfate gradient. Dfh eluted at 800 mM ammonium sulfate. Following an additional dialysis step, the final purification stage utilized a Sephacryl 75 size-exclusion column equilibrated with 20 mM HEPES and 10 mM $MgSO_4$ (pH 7.0). Freshly isolated protein was degassed on a Schlenk line and stored under positive argon pressure at 4 °C in 20 mM HEPES (pH 7.0), 10 mM $MgSO_4$, and 5 mM β-mercaptoethanol. Under these conditions, the protein was stable for more than 2 weeks against degradation and precipitation.

The Isu1 mature processed protein sequence (beginning at amino acid 35 of the open reading frame) was amplified by PCR from *Saccharomyces cerevisiae* strain YPH499. The sites for restriction enzymes NdeI (5′) and XhoI (3′) were added during PCR to facilitate subsequent manipulations, and the amplified fragment was cloned into pET21b, thereby adding a His6 tag to the C-terminus of the open reading frame. The plasmid was sequenced, and the insert sequence matched that deposited in the SGD database for Isu1. The Isu expression plasmid was transformed into *E. coli* cells [BL21(DE3) codon plus] and induced according to standard protocols. The expressed protein was found to be highly expressed but located primarily in inclusion bodies. The D37A mutant (changing amino acid 37 of the mature protein from aspartate to alanine) was constructed by site-directed mutagenesis (QuickChange, Stratagene), and the expressed protein in this case was more soluble and less prone to aggregation during purification. Analogous mutant Isu homologues in *Azotobacter vinelandii* (30) and *Schizosaccharomyces pombe* (31) were loaded normally, indicating that the mutation does not interfere with formation of the [2Fe-2S] cluster scaffold intermediate. For these experiments,

the BL21 cells expressing the mature Isu1-His6 with the D37A mutation were grown in rich medium with plasmid selection (chloramphenicol and ampicillin) and induced according to the autoinduction method described by Studier (32). Cells were lysed using a French press and sonicated. Protein isolation followed a two-step protocol. A prepacked His-prep FF nickel affinity column (Pharmacia) was pre-equilibrated with 100 mM sodium phosphate buffer (pH 7.5) containing 300 mM sodium chloride and 20 mM imidazole. After the protein was loaded on the column, it was eluted with an imidazole gradient (from 20 to 500 mM imidazole). Isu eluted at ca. 20% imidazole. Protein was then dialyzed in HEPES buffer [20 mM HEPES and 150 mM sodium chloride (pH 7.5)], concentrated, and passed through a Sephacryl 75 size-exclusion column (Pharmacia) to yield pure protein. Pure Isu was colorless and completely lacking Fe–S cofactor.

Dfh Fold and Stability

Experiments directed at determining apo-Dfh's fold, as well as its thermal and chemical stability, were performed. CD spectra of Dfh [20 μM protein in 5 mM sodium phosphate buffer (pH 7.5)] were recorded at 25 °C over a wavelength range of 190–260 nm using a temperature-regulated Olis CD spectrometer. Spectra were recorded at 1.0 nm resolution and baseline corrected by subtraction of the buffer spectrum. Quantitative estimates of the individual secondary structure components in the Dfh CD spectra were obtained through simulations using Olis's software analysis package modified to include the variable selection of reference proteins in a locally linearized model (33). Thermal unfolding curves were obtained by monitoring the ellipticity at both 208 and 222 nm using 1 mm path length cells. Samples were heated in 2.5 °C increments at a rate of 1 °C/min over the temperature range of 10–90 °C. Thermal unfolding was analyzed, and the protein's melting temperature, T_M, was calculated using a two-state model for unfolding.

Chemical denaturation studies were performed on apo-Dfh to determine the energetic stability of the protein. Fluorescence studies were performed on Dfh incubated in 20 mM HEPES and 10 mM $MgSO_4$ (pH 7) with increasing amounts of urea (Sigma). Independent samples exposed to urea concentrations between 1 and 6 M were kept at 23 °C for 3 h. Intrinsic fluorescence emission spectra were recorded between 300 and 400 nm following excitation at 280 nm. Slit widths were set at 4.0 nm. The red shifts in intrinsic fluorescence emission spectra at increasing urea concentrations were quantified as the intensity-averaged emission wavelength, λ_{avg}, calculated according to eq 1.

$$\lambda_{avg} = \sum(I_i \lambda_i) / \sum(I_i) \quad (1)$$

where (λ_i) and I_i are the emission wavelength and its corresponding fluorescence intensity at that wavelength, respectively. Baseline and transition region data for the first and second component of the Dfh–urea equilibrium denaturation curve were fit to a two-state linear extrapolation model according to eq 2.

$$\Delta G_{unfolding} = \Delta G^{H_2O} - m[D] = -RT \ln K_{unfolding} \quad (2)$$

In eq 2, $\Delta G_{unfolding}$ is the free energy change for unfolding at a given denaturant concentration, $\Delta G^{H2}O$ is the free energy change for unfolding in the absence of denaturant, m is a slope term that equates the change in $\Delta G_{unfolding}$ per unit concentration of urea [D], R is the gas constant (1.987 cal mol^{-1} K^{-1}), T is the temperature (296.15 K), and $K_{unfolding}$ is the equilibrium

constant for unfolding. The linear extrapolation model expresses the signal (averaged emission wavelength, λ_{avg}) as a function of urea concentration in a manner described elsewhere (34).

Characterization of Protein Oligomeric State

Size-exclusion chromatography was used to determine the oligomeric state of apo- and holo-Dfh. Apo-Dfh samples were prepared in 20 mM HEPES buffer (pH 7.0) in the presence of 10 mM $MgSO_4$. Holo-Dfh, at a ferrous iron:protein stoichiometry of 12:1, was prepared by combining concentrated buffered protein and ferrous ammonium sulfate (Sigma) solutions. As a salt-dependent control, an iron-loaded Dfh sample was prepared without any magnesium salt. All solutions were made anaerobic prior to mixing by repeated vacuum and argon(g) purging cycles on a Schlenk line. Solutions were stored and transported under argon pressure by capping all glassware using airtight septa. Iron-loaded samples were prepared in a nitrogen(g)-filled glovebox (Plas Laboratories, Lansing, MI). Apo- and holo-Dfh samples were individually loaded, using an anaerobic syringe, onto a Sephacryl S-75 high-resolution size-exclusion column pretreated with 2 column volumes of the corresponding argon-purged buffer. Protein controls of anaerobic buffered vitamin B_{12} (1.3 kDa), myoglobin (17 kDa), ovalbumin (44 kDa), γ-globulin (158 kDa), and thyroglobulin (670 kDa) were used as molecular size standards (Bio-Rad).

Substrate and Protein Partner Binding Characteristics

Frataxin's iron binding affinity and maximal metal:protein stoichiometry were determined by ITC. Protein and aqueous ferrous ammonium sulfate solutions were prepared anaerobically in 20 mM HEPES (pH 7.0) and 10 mM $MgSO_4$. ITC experiments were conducted anaerobically at 30 °C using a VP-ITC titration microcalorimeter (MicroCal, Inc.) by titrating a 1.2 mM ferrous iron solution into a 1.4 mL volume of a 100 μM protein solution. Following an initial 2 μL iron solution injection, 29 additional injections of 10 μL each were titrated into the protein sample. The period between injections was 10 min, and the syringe stirring speed was held constant at 500 rpm. All experiments were conducted in triplicate on independent protein and iron samples to ensure data reproducibility. Data analysis was performed utilizing the Origin 7.0 Scientific Graphing and Analysis Software (provided by MicroCal) by applying a nonlinear least-squares curve-fitting algorithm to determine the stoichiometric ratio, dissociation constant, and change in enthalpy or entropy for iron bound to Dfh.

The binding affinity of apo- and holo-Dfh for the yeast Isu1 D37A mutant was also tested by ITC. Dfh loaded with a single iron atom was prepared anaerobically in 20 mM HEPES (pH 7.5) and 150 mM sodium chloride at a protein concentration of 600 μM. A 50 μM solution of apo-Isu1 was prepared anaerobically in the same buffer. Following an initial 2 μL holo-Dfh injection, 29 additional injections of 10 μL each were titrated into Isu. The period between injections was 10 min, and the syringe stirring speed was held constant at 500 rpm. All experiments were repeated in triplicate on independent protein and iron samples to ensure the reproducibility of the data. Data analysis was performed as outlined above.

Oxidative Degradation Assay

Experiments directed at assessing Dfh's ability to moderate the formation of free oxygen radicals produced as a result of Fenton chemistry were performed. In the presence of aqueous ferrous iron and peroxide, deoxyribose sugar is rapidly degraded to malondialdehyde (MDA) as a result of Fenton chemistry. MDA concentrations can be monitored spectrophotometrically at 532 nm ($\Sigma_{532} = 1.54 \times 10^5\ M^{-1}\ cm^{-1}$) from the chromophore produced in the presence of thiobarbituric acid (35). The ability of Dfh to attenuate Fenton chemistry was tested under the following conditions: 48 μM Fe(II), 24 μM H_2O_2, and/or 5 mM 2-deoxyribose sugar were incubated in 20 mM HEPES and 10 mM $MgSO_4$ (pH 7.0) in the presence or absence of 96 μM Dfh (final volume of 200 μL) for 30 min at 30 °C. Aliquots with 200 μL of 4% phosphoric

acid and 200 μL of 1% thiobarbituric acid were successively added, and the samples were boiled for 15 min. Samples were cooled at 0 °C for 3 min; 75 μL of 10% SDS was then added, and the optical density at 532 nm was immediately recorded on a Cary UV–vis spectrophotometer (36). Experiments were performed on identical reproducible samples.

Characterization of Bound Iron's Electronic and Structural Properties

X-ray absorption spectroscopy was utilized to investigate the electronic characteristics and ligand coordination geometry of iron bound to Dfh. Multiple independent holo-Dfh samples were prepared in a nitrogen-purged glove-box with a single bound iron. Samples were prepared in 20 mM HEPES buffer (pH 7.0), 10 mM $MgSO_4$, and 30% glycerol, yielding a final iron concentration of 1 mM. Samples were loaded into Lucite XAS cells wrapped with Kapton tape, flash frozen in liquid nitrogen, removed from the glovebox, and stored in liquid nitrogen. XAS data were collected at the Stanford Synchrotron Radiation Laboratory (SSRL), on beamline 7-3, and at the National Synchrotron Light Source (NSLS), beamline X3-b. Beamline 7-3 was equipped with Si(220) double-crystal monochromator, while beamline X3-b was equipped with a Si(111) single-crystal monochromator. Both beamlines were equipped with harmonic rejection mirrors. During data collection, samples were maintained at 10 K using an Oxford Instruments continuous-flow liquid helium cryostat at SSRL and at ca. 24 K using a helium Displex Cryostat at NSLS. Protein fluorescence excitation spectra were collected using a 30-element germanium solid-state array detector at SSRL and a 13-element germanium solid-state array detector at NSLS. XAS spectra were measured using 5 eV steps in the pre-edge region (6900–7094), 0.25 eV steps in the edge region (7095–7135 eV), and 0.05 $Å^{-1}$ increments in the extended X-ray absorption fine structure (EXAFS) region (to k = 13.5 $Å^{-1}$), integrating from 1 to 20 s in a k^3-weighted manner for a total scan length of approximately 40 min. X-ray energies were calibrated by recording an iron foil absorption spectrum simultaneously with collection of protein data. The first inflection point for the iron foil edge was assigned at 7111.3 eV. Each fluorescence channel of each scan was examined for spectral anomalies prior to averaging. SSRL protein data represent the average of five or six scans, while NSLS protein data represent the average of nine to ten scans.

XAS data were processed using the Macintosh OS X version of the EXAFSPAK program suite integrated with Feff version 7.2 for theoretical model generation (37,38). Data reduction and processing of pre-edge transitions followed previously established protocols (20). Analysis of X-ray absorption near-edge spectroscopy (XANES) 1s → 3d transitions was completed using the EDG_FIT subroutine within EXAFSPAK (38). Only spectra collected using the higher-resolution Si(220) monochromator crystals were subjected to edge analysis. EXAFS fitting analysis was performed on raw/unfiltered data following our published protocol (20). EXAFS data were fit using both single- and multiple-scattering theoretical amplitude and phase functions for iron–oxygen/nitrogen, iron–sulfur, and iron–iron interactions calibrated utilizing published iron model data as our controls. During spectral simulations, metal–ligand coordination numbers were fixed at half-integer values, while only the absorber–scatterer bond length (R) and Debye–Waller factor (σ^2) were allowed to freely vary.

Fe–Cofactor Assembly Assays

The ability of Dfh to serve as an iron chaperone during Fe–S cluster assembly was tested using the apo-Isu1 D37A cofactor assembly enzyme as the binding partner. All protein and substrate samples were made anaerobic on an Schlenk line and stored under positive argon pressure. Dfh was incubated with ferrous ammonium sulfate at a metal:protein ratio of 1:1 for 20 min at 30 °C. Fe–S cluster assembly was initiated by addition of ferrous iron directly, or as part of the holo-Dfh complex, to a 500 μL solution containing 100 μM Isu1, 4.3 mM DTT, and 2.4 mM sodium sulfide. The final Fe concentration was 100 μM, and all samples were buffered in 20 mM HEPES and 150 mM NaCl (pH 7.5). Controls with Isu or Dfh alone and with Isu or

Dfh, DTT, and sodium sulfide were prepared under the same conditions listed above. Fe–S cluster assembly was monitored using UV–visible absorption spectroscopy. Absorption spectra between 200 and 600 nm were recorded. A time course for the reaction progress was prepared by spectral detection every 30 s using the spectral wavelength of 426 nm(a chromophore characteristic for [2Fe-2S]clusters)(11,39). Assembly spectra were collected to completion for up to 1 h on three independent samples to test the reproducibility of data. The average time dependence data for Fe–S cluster formation for each condition were fit with a rate equation for a first-order assembly process to estimate a value of the average assembly rate (k_{obs}) (39).

RESULTS

Dfh Fold and Stability

Dfh is a highly stable protein, and structural evidence indicates it is well-folded. The 133-amino acid mature *Drosophila* protein was expressed at high levels in bacteria (50 mg/L of medium). Mass spectrometric analysis of apo-Dfh indicates a molecular mass of 15157 Da. Unlike the yeast frataxin homologue Yfh1 (20), apo-Dfh was highly stable against autodegradation and aggregation for extended periods of time when stored anaerobically at either −20 or 4 °C. Unlike that of human frataxin, Dfh's N-terminus was stable against autodegradation. Spectral features in the Dfh CD spectra are clearly apparent for both α-helical and *β*-strand secondary structural elements [Figure 1 of the Supporting Information (SI)]. CD spectral simulations yielded approximate secondary structural contents of 19 ± 7% α-helix, 33 ± 7% *β*-sheet, 18 ± 7% turns, and 30 ± 7% unfolded residues. CD spectral features and simulated fold characteristics for Dfh are consistent with the α–*β* sandwich motif structure observed for the structurally characterized frataxin orthologs (see the review in reference 40).

A melting temperature for Dfh was determined using CD spectroscopy. Full CD spectra for Dfh, covering the wavelength range of 190–260 nm, were collected over a broad temperature range to generate a thermal denaturation profile. Thermal profiles, generated for two independent samples, were determined by measuring changes in molar ellipticity at both 208 and 222 nm. A representative plot of the temperature-dependent fractional fold of the protein, utilizing the 10 and 90 °C spectra as limits, is given for the 208 nm signals in Figure 1A. Fits to the Dfh thermal denaturation profile (Figure 1A, solid line) gave a melting temperature of 59.2 ± 2.4 °C. This value is close to the T_M of 65 °C obtained for N-terminally truncated mature human frataxin (residues 91–210) but significantly higher than the published value of ca. 44 °C for mature yeast frataxin (41).

Urea denaturation studies were used to measure the conformational stability of Dfh. Pure apoprotein was subjected to extensive incubation with increasing concentrations of urea. Fluorescence signals from aromatic residues were then used to measure variations in the protein's fold. This change in intrinsic fluorescence is manifested as a red shift in maximal emission wavelength. The intensity-averaged emission wavelength (λ_{avg}), an integral measurement that is negligibly influenced by noise, was calculated and plotted versus urea concentration (Figure 1B). Values for ΔG^{H_2O} and m were obtained by fitting the data to the model described earlier representing a direct transition from a folded to a denatured state (34). The conformational stability of Dfh (ΔG^{H_2O} = 7.44 ± 0.47 kcal/mol) is similar to the reported range for human frataxin (5.7–8.5 kcal/mol) (42). $[D]_{50\%}$ is the denaturant concentration at the midpoint of the transition where $K_{unfolding}$ = 1 (the amount of unfolded protein is equal to the amount of folded protein). $[urea]_{50\%}$ for Dfh is 2.37 ± 0.23 M which is more stable than our recent unpublished measurement for yeast frataxin (1.72 ± 0.22 M) but lower than the value obtained for human frataxin (4.3 M) (42). From eqs 1 and 2, it follows that

$$\Delta G^{H_2O} = m[D]_{50\%} \quad (3)$$

where the slope term *m* is proportional to the surface area of the protein exposed to the solvent upon unfolding (43). Dfh has an *m* value of 3.13 ± 0.20 kcal mol^{-1} M^{-1} that is higher than the unpublished value obtained for yeast frataxin (*m* = 1.60 ± 0.13 kcal mol^{-1} M^{-1}). A lower *m* value for yeast frataxin compared to that of Dfh suggests that, during the unfolding process, there may exist a transient folding conformation for the yeast protein whose surface area is more accessible to the chaotrope (43). Values of *m* from 1.36 ± 0.05 to 5.35 ± 0.33 kcal mol^{-1} M^{-1} have been reported for human frataxin depending on the kind of denaturant used (42). Deviation from the two-state mechanism may lower the *m* value, and there is always a possibility of different unfolding intermediates being formed under different denaturation conditions. We have used multiple spectral probes (CD, fluorescence), and the unfolding curves are consistent with a two-state mechanism for Dfh.

Iron and Protein Partner Binding Characteristics of Dfh

Size-exclusion chromatography was employed to determine the oligomeric state of Dfh in the presence and absence of ferrous iron, as well as to test the effect of salt on the protein's oligomeric state. In the presence of 10 mM $MgSO_4$ and under anaerobic conditions, both apo-Dfh and iron-loaded Dfh are stable protein monomers that elute at a projected size of ca. 17 kDa (Figure 2 of the SI). In the absence of salt, Dfh exposed to excess Fe(II) is however partially (5% based on Bradford assays) promoted to a higher-order molecular mass with an estimated size of ca. 120 kDa. The presence of Mg(II) salt clearly influences the protein's aggregation state under extreme iron-loaded conditions, stabilizing the protein as a holo monomer.

ITC was used to characterize the ferrous iron binding affinity and maximal metal:protein stoichiometry of iron to monomeric Dfh. ITC was also used to estimate the binding affinity and stoichiometry of holo-Dfh and Isu. Changes in heat associated with the anaerobic addition of ferrous iron to Dfh are shown in the raw ITC data (Figure 2A). These raw ITC data are consistent with an exothermic iron binding event. Iron binding follows an exponential binding curve in the early stages, followed by a constant heat release pattern consistent with simple iron dilution in the postsaturation state. The best fit binding isotherm (Figure 2B) is consistent with Dfh binding 1.0 ± 0.2 ferrous iron atoms per protein monomer with a micromolar binding affinity (K_d = 6.0 ± 0.2 μM). Binding of the metal to Dfh is enthalpically (ΔH = −28.5 ± 6.9 kcal/mol) but not entropically (ΔS = −70.2 ± 22.9 cal K^{-1} mol^{-1}) favorable. Heat release profiles during protein complex formation (Figure 2C) show holo-Dfh interacts with Isu also in an exothermic pattern. Iron is required for protein complex formation (data not shown). The total energy plot (Figure 2D) was best simulated by a two-stage binding model, consistent with an average binding stoichiometry of 0.90 ± 0.08 for the holo-Dfh monomer per Isu monomer. The curve fitting analysis gave a binding affinity of holo-Dfh to Isu1 in the nanomolar range (average K_d = 210 ± 14 nM), and protein binding is again enthalpically (ΔH = −25.3 ± 11.5 kcal/mol) but not entropically (ΔS = −51.8 ± 39.9 cal K^{-1} mol^{-1}) favorable.

Attenuation of Fenton Chemistry

Dfh was tested for its ability to attenuate Fenton chemistry, an ability exhibited by other frataxin orthologs (36). To test this ability, we measured the extent of oxidative degradation of 2-deoxyribose to its oxidized product malondialdehyde (MAD) in the presence of ferrous iron and hydrogen peroxide. Control experiments with peroxide in the absence of metal did not result in a significant production of MAD (Figure 5, lane 5), indicating oxidative damage results from iron-promoted generation of reactive oxidative species. An additional control with iron in the absence of hydrogen peroxide showed simple iron oxidation in an aerobic environment

can generate sufficient ROS to produce MAD (Figure 3, lane 1). In the absence of Dfh but with peroxide and iron present, substantial formation of MAD (2.46 ± 0.30 μM) was observed. In the presence of Dfh, levels of MAD produced over the same time duration (1.2 ± 0.41 μM) were half those observed in the absence of frataxin (Figure 5, lanes 3 and 4). Iron-loaded Dfh in the absence of peroxide (Figure 5, lane 2) has a minimal effect on MAD generation.

Electronic and Coordination Properties of Protein-Bound Iron

XAS studies were used to characterize the electronic and structural properties of iron bound to Dfh. Iron K-edge XANES spectra of holo-Dfh, compared to Fe(II) and Fe(III) controls (20), are given in Figure 3 of the Supporting Information. General edge features for frataxin-bound iron resemble those observed for the Fe(II) control. The first inflection edge energy for iron bound to Dfh closely matches that obtained for the Fe(II) control (7122.42 ± 0.05 eV and 7122.90 ± 0.03 eV, respectively), as compared to the value obtained for the Fe(III) control (7126.30 ± 0.02 eV), indicating Dfh-bound iron is stable in the ferrous state. Analysis of the 1s → 3d electronic transition in the Dfh iron XANES, a feature highly correlated to metal–ligand symmetry and iron spin state, gave a unitless area of 7.61 ± 0.06 with individual transitions at 7111.40, 7112.22, and 7113.76 eV. This overall transition area is slightly larger than those observed previously for ferrous ion bound to yeast and human frataxin, and our ferrous control (values of 5.46 ± 0.07, 5.20 ± 0.50, and 5.18 ± 0.015, respectively) (20,40). The transition energies and overall area are consistent with a partially symmetric six-coordinate Fe(II) ligand environment, although the ligand environment in Dfh is less symmetric than those in frataxin orthologs. Iron bound to Dfh is stable in the high-spin state.

EXAFS analysis was used to provide the metal–ligand metric parameters for ferrous iron bound to Dfh. Raw EXAFS data for Fe(II) bound to Dfh (Figure 4A) show a single frequency pattern with a maximum amplitude at 5.5 $Å^{-1}$, indicating the iron–ligand coordination environment is fairly symmetric and dominated by a single ligand scattering environment constructed of oxygen and/or nitrogen atoms. The Fourier transform of the raw EXAFS data for Fe(II)-bound Dfh (Figure 4B) also suggests ligand scattering is constructed from a single set of nearest-neighbor scattering ligands. EXAFS simulations confirm the nearest-neighbor coordination geometry is dominated by oxygen/nitrogen-based ligands directly coordinated to the iron at an average bond length of 2.13 Å (Table 1, fit 1). Any attempt to fit the Dfh Fe-EXAFS with a contribution from sulfur scattering, or even with two independent nearest-neighbor ligand environments, was not statistically justified in our data analysis (Table 1, fits 2–4, respectively). The average Fe–O/N bond length matches the averaged distance obtained for six-coordinate Fe(II)–O model compounds listed in the Cambridge Structural Database (44). The reduced coordination number (CN = 5) observed for the Fe–O/N fits for iron coordinated to Dfh is most likely a reflection of the lack of complete symmetry in the six individual Fe–O/N bond vectors for protein-coordinated metal. An additional indication of partial bond asymmetry in the nearest-neighbor ligand geometry is the high Debye–Waller factor (5.23×10^{-3} $Å^2$) observed for this simulation. Although long-range scattering is observed when $R > 3$ Å in the Fourier transform, this feature could not be justifiably fit.

Fe–Cofactor Assembly Assay

We tested the ability of holo-Dfh to deliver the Fe(II) required for enzymatic Fe–S cluster biosynthesis. Following a published protocol (11) modified by our laboratory, Dfh loaded with a single Fe(II) atom (protein concentration of 100 μM) was added to a reaction mixture consisting of 100 μM D37A Isu1 incubated with DTT (4.3 mM). Experiments were performed with excess (2.4 mM) sodium sulfide. Assembly of [2Fe-2S] clusters was monitored spectrophotometrically, using UV–visible spectroscopy, by the increase in the characteristic cluster absorption bands over the range of 300–600 nm (45,46). The principle absorption band centered at 426 nm was used to correlate Fe–S cluster production. Assembly was monitored

following strict anaerobic procedures. In the absence of both proteins, an aqueous solution of ferrous iron, sodium sulfide, and DTT showed the time-dependent formation of a black precipitate with no 426 nm spectral signal. Additional controls with Isu or Dfh alone, Isu or Dfh with DTT and sodium sulfide, and Isu or Dfh with DTT and Fe(II) also did not show any Fe–S cluster formation, based on the lack of a 426 nm signal (data not shown). Isu in the presence of DTT and both sulfide and ferrous iron showed a subtle buildup of soluble [2Fe-2S] clusters over 1 h, as indicated by the slight increase in the magnitude of the 426 nm absorption signal (Figure 5B). After 1 h, the final solution was precipitate free. When iron-loaded Dfh was used as the metal source, there was a substantial buildup of Isu-catalyzed [2Fe-2S] clusters over the 1 h time duration (Figure 5A). A simulation of the Dfh-enhanced [2Fe-2S] formation time profile using a first-order rate equation gave a k_{obs} of 0.096 min^{-1}. This value is similar to that obtained for human frataxin (k_{obs} = 0.075 min^{-1}) (11). Again after 1 h, there was no noticeable precipitate.

DISCUSSION

Our results support the idea that frataxin is an iron binding protein that delivers ferrous iron to the iron–sulfur assembly apparatus scaffold during [2Fe-2S] cluster biosynthesis. Beginning with the initial report showing that frataxin is an iron binding protein (16), numerous NMR reports have identified the conserved acidic residues in the protein's helix 1 and strand 1 regions as the most likely candidates for iron binding residues (20,21,47). An established connection between frataxin and in vivo cellular Fe–S cluster biosynthesis, coupled with the observation that frataxin directly interacts with Fe–S cluster assembly enzymes, further highlights the functional requirement for frataxin-mediated iron delivery during Fe–cofactor assembly (4,5, 7–10).

The bulk of the in vitro biophysical data establishing a molecular understanding of frataxin's iron binding and delivery properties has come from the yeast, human, and bacterial orthologs (11,19–22,36,47–50). Issues regarding the instability of frataxin toward N-terminal autodegradation (in the human protein) or the high susceptibility for oxidative damage-induced aggregation (in the yeast frataxin ortholog) have plagued studies on the eukaryotic orthologs. The enhanced stability of *Drosophila* frataxin compared to the other eukaryotic orthologs suggests that the fly model may be a more attractive system for in vitro studies of frataxin's function. Dfh is better behaved in terms of in vitro storage artifacts. Although the reasons for this are not entirely clear, the protein is more stable and less prone to damage and secondary changes during storage. This is a great help for Fe–S cluster synthesis assays and other in vitro biochemical studies. Furthermore, Dfh is less prone to aggregation than the yeast protein. The field has been confounded by this issue. It seems that there are tremendous differences from species to species in terms of the tendency of frataxins to form metal-dependent oligomers. The in vivo function of this oligomerization process is questionable in view of the Craig yeast mutant which shows normal function and no oligmerization (51). The ability to study Dfh function without dealing with oligomerization is a great asset. Finally, Dfh is more stable toward unfolding than the yeast ortholog. Structure–function analysis correlating mutant forms of Dfh with function will therefore be more readily accomplished with a more stable protein. We have found that mutations that destabilize yeast frataxin in vivo lead to protein degradation and thus cannot be interpreted in terms of their effects on frataxin function (data not shown). Finally, Dfh is stable against N-terminal degradation, making it a more attractive candidate for characterizing protein function as compared to the other multicellular eukaryotic ortholog. It is for these reasons that we have performed a comprehensive in vitro characterization of Dfh's iron binding and delivery properties.

Although there are differences in the overall stability of the frataxin orthologs, our initial qualitative structural characterization of Dfh suggests the protein has the same overall fold as

the orthologs. The measured percentages of secondary structural elements that dictate Dfh's fold match the α–*β* sandwich motif structure determined from other frataxin orthologs (reviewed in reference 40). Like that of the yeast ortholog, the N-terminus of mature Dfh is highly stable against cleavage; the pure as-isolated apo-Dfh is even more stable than apo-Yfh1 against autodegradation (20). The thermal stability of Dfh (T_M = 59.2 ± 2.4 °C) more closely resembles that of the human ortholog (T_M 65 °C), most likely as a reflection of the fact that both proteins have extensive C-terminal tails that positively influence protein stability (41). Interestingly, while the T_M values measured for the human and fly frataxin orthologs are very similar, the chemical stability of Dfh toward unfolding in the presence of denaturants is slightly reduced compared to that of the human protein. Similarities in ΔG^{H_2O} and *m* values for Dfh and the human protein obtained from chemical denaturation studies suggest similar mechanisms for unfolding between the two orthologs.

Numerous reports have shown that frataxin orthologs can aggregate at high iron concentrations, suggesting an alternative function of the protein for serving as an iron storage system that can control available metal levels and the subsequent formation of ROS that would surely be produced under mitochondrial iron overload conditions (16,36,48,52). However, the presence of salt and stoichiometric iron levels negatively influence protein oligomerization (17,20,40). The facts that mutations which prevent frataxin oligomerization have no in vivo Fe–cofactor production phenotypes under normal growth conditions (51) and that in vitro activity assays for Fe–S cluster assembly show monomeric holofrataxin delivers Fe(II) to Isu (11) underline the point that the monomeric holoprotein is most likely the iron chaperone during Fe–S cluster assembly. In the presence of salt, Dfh loaded with a 12-fold excess of Fe(II) is stable as a holoprotein monomer, indicating under these solution conditions we can adequately characterize the iron binding and delivery properties of monomeric holo-Dfh.

The iron binding affinity and optimal metal:protein stoichiometry of monomeric Dfh were characterized to elucidate the biophysical details of iron binding by Dfh. In addition, the capacity of monomeric holo-Dfh to bind to the yeast Isu ortholog was characterized to provide relevant biophysical details for our Fe–cofactor assembly activity assay. Under the solution conditions we tested, Dfh can bind approximately 1 equiv of Fe(II) with a binding affinity (K_d) of ≈6.0 μM. Under identical solution conditions, yeast frataxin binds two iron atoms with a similar affinity (averaged K_d of 2.5 μM) (20). Similar binding affinities were also measured for human and bacterial frataxin (K_d values of 55.0 and 3.8 μM, respectively), although at variable metal binding stoichiometries (11,18). As previously reported for human frataxin (11), Dfh interacts with Isu in an iron-dependent manner. A binding stoichiometry of 0.90 ± 0.08 and a binding affinity of ca. 0.21 μM also closely match the values of 0.95 and ca. 0.15 μM, respectively, obtained between the human proteins, and in both cases, binding is energetically favorable (11). It is important to note that holo-Dfh was able to interact with the yeast Isu. The presence of the D37A mutation in the yeast Isu protein utilized for these studies would be unlikely to alter the rates of formation of scaffold intermediates, as previous work has shown for *Azotobacter* and *S. pombe* Isu homologues. The facts that the Dfh binding affinity, binding energy, and stoichiometry with respect to Isu so closely match those seen for complementary proteins in the human system and that [2Fe-2S] cluster assembly activity is observed between Dfh and Isu1 only further emphasize the idea that the functional role of frataxin toward Fe–S cluster biosynthesis is conserved between organisms.

Frataxin can protect DNA against H_2O_2-driven oxidative degradation by attenuating the Fenton chemistry promoted in the presence of aqueous Fe(II). This property was first identified for the yeast frataxin ortholog (36), and our studies show that Dfh also provides a significant enhancement in stability for deoxyribose sugars against oxidative degradation in the presence of Fe(II) and H_2O_2. In *Drosophila*, frataxin has been suggested to play a direct role in controlling cellular oxidative stress (27,28). In addition, overexpression of catalase completely

compensated for the adverse oxidative damage caused under frataxin deficient conditions (29). These data suggest that H_2O_2 is an important pathogenic substrate that underlies the phenotypes observed in FRDA cells (29). The ability of frataxin to directly regulate Fenton chemistry is clearly an additional and highly important function both directly and indirectly correlated to Fe–S cluster bioassembly.

Ferrous iron bound to Dfh is high-spin and coordinated in a ligand environment constructed by only oxygen/nitrogen ligands. Pre-edge transition energies and areas determined from the Fe k-edge XANES spectrum for holo-Dfh are similar to those observed for monomeric Fe(II)-loaded human and yeast frataxin (20,53) and closely resemble the values obtained for partially symmetric high-spin six-coordinate Fe(II) model compounds (54,55). Metric parameters obtained from EXAFS analysis indicate the metal–ligand coordination environment for Fe(II) bound to Dfh is constructed completely with oxygen- and nitrogen-based ligands. While the technique cannot directly distinguish between oxygen- and nitrogen-based ligands, the technique can yield bond length with a very high degree of accuracy (±0.02 Å) (56). These accurate values can then be used to provide insight into probable coordination ligand types and geometries. The average nearest-neighbor bond length (2.13 Å) obtained for Fe(II) bound to Dfh is close to the average value obtained from all Fe(II)–O_6 small molecules (2.14 Å) published in the Cambridge Structural Database (44). An Fe(II)–O_6 nearest-neighbor environment in Dfh is in direct agreement with the coordination environment observed for the other monomeric holofrataxin orthologs (20,53) and consistent with the identification of conserved acid residue side chains serving as the iron binding ligands in all frataxin orthologs (20,21,40,47,50). While the bulk of the six oxygen ligands most likely come from carboxylate oxygens from the conserved acidic residues in the protein's helix 1 and strand 1 structural elements (40), water is most certainly a ligand contributing to protein-bound iron. In addition, the fact that Dfh-bound Fe(II) is in a partially symmetric six-coordinate ligand environment may be the key to how the protein attenuates metal reactivity toward Fenton chemistry and not just the binding affinity (e.g., EDTA does not attenuate, desferrioxamine does).

Evidence supporting frataxin's role as an iron chaperone during Fe–S cluster biosynthesis is further strengthened by the observation that frataxin actively stimulates cofactor production. When delivery of Fe(II) to Isu is mediated by Dfh, there is a significant enhancement in Fe–S cluster production compared to that under conditions in which frataxin is absent. The tight binding affinity between holo-Dfh and Isu confirms a binding event occurs between the two proteins, so it is tempting to suggest that simple complex formation could promote in vivo metal delivery. A weak binding affinity of iron for Dfh relative to the tighter affinity of holo-Dfh for Isu may imply that iron binding to frataxin provides a signal for formation of an assembly complex. Interestingly, this binding affinity is shared between partners from different organisms. Our identification of two unique yeast frataxin Fe(II) binding sites, one utilizing surface-exposed acidic residues on the protein's helix 1 and the other on the opposite face of the planar molecule utilizing conserved acidic residues on strands 1 and 2, may indicate metal bound to one of the two sites may be specific for the delivery of metal to Isu (20). However, the mechanism for direct metal transfer between frataxin and Isu remains unclear, specifically with regard to multiprotein complex formation with the cysteine desulfurase and Isd11. Furthermore, the fact that frataxin deletion in *S. cerevisiae* still allows some level of in vivo production of [2Fe-2S] clusters suggests that alternative frataxin-independent mechanisms of iron delivery exist (57). While the exact molecular details of the complete enzymatic pathway still remain elusive, our results clearly indicate that frataxin can bind and deliver the Fe(II) required for Fe–S cluster biosynthesis.

Supplementary Material

Refer to Web version on PubMed Central for supplementary material.

Acknowledgements

Portions of this research were carried out at both the Stanford Synchrotron Radiation Laboratory (SSRL) and the National Synchrotron Light Source (NSLS). SSRL is a national user facility operated by Stanford University on behalf of the U.S. Department of Energy, Office of Basic Energy Sciences. The SSRL Structural Molecular Biology Program is supported by the Department of Energy, Office of Biological and Environmental Research, and by the NIH, National Center for Research Resources, Biomedical Technology Program. NSLS, located at Brookhaven National Laboratory, is supported by the U.S. Department of Energy, Division of Materials Sciences and Division of Chemical Sciences, under Contract DE-AC02-98CH10886.

References

1. Campuzano V, Montermini L, Molto MD, Pianese L, Cossee M, Cavalcanti F, Monros E, Rodius F, Duclos F, Monticelli A, Zara F, Canizares J, Koutnikova H, Bidichandani SI, Gellera C, Brice A, Trouillas P, De Michele G, Filla A, De Frutos R, Palau F, Patel PI, Di Donato S, Mandel JL, Cocozza S, Koenig M, Pandolfo M. Friedreich's ataxia: Autosomal recessive disease caused by an intronic GAA triplet repeat expansion. Science 1996;271:1423–1427. [PubMed: 8596916]
2. Babcock M, de Silva D, Oaks R, Davis-Kaplan S, Jiralerspong S, Montermini L, Pandolfo M, Kaplan J. Regulation of mitochondrial iron accumulation by Yfh1p, a putative homolog of frataxin. Science 1997;276:1709–1712. [PubMed: 9180083]
3. Cossee M, Puccio H, Gansmuller A, Koutnikova H, Dierich A, LeMeur M, Fischbeck K, Dolle P, Koenig M. Inactivation of the Friedreich ataxia mouse gene leads to early embryonic lethality without iron accumulation. Hum Mol Genet 2000;9:1219–1226. [PubMed: 10767347]
4. Muhlenhoff U, Richhardt N, Ristow M, Kispal G, Lill R. The yeast frataxin homolog Yfh1p plays a specific role in the maturation of cellular Fe/S proteins. Hum Mol Genet 2002;11:2025–2036. [PubMed: 12165564]
5. Rotig A, de Lonlay P, Chretien D, Foury F, Koenig M, Sidi D, Munnich A, Rustin P. Aconitase and mitochondrial iron-sulphur protein deficiency in Friedreich ataxia. Nat Genet 1997;17:215–217. [PubMed: 9326946]
6. Koutnikova H, Campuzano V, Foury F, Dolle P, Cazzalini O, Koenig M. Studies of human, mouse and yeast homologues indicate a mitochondrial function for frataxin. Nat Genet 1997;16:345–351. [PubMed: 9241270]
7. Puccio H, Simon D, Cossee M, Criqui-Filipe P, Tiziano F, Melki J, Hindelang C, Matyas R, Rustin P, Koenig M. Mouse models for Friedreich ataxia exhibit cardiomyopathy, sensory nerve defect and Fe-S enzyme deficiency followed by intramitochondrial iron deposits. Nat Genet 2001;27:181–186. [PubMed: 11175786]
8. Chen OS, Hemenway S, Kaplan J. Inhibition of Fe-S cluster biosynthesis decreases mitochondrial iron export: Evidence that Yfh1p affects Fe-S cluster synthesis. Proc Natl Acad Sci USA 2002;99:12321–12326. [PubMed: 12221295]
9. Duby G, Foury F, Ramazzotti A, Herrmann J, Lutz T. A non-essential function for yeast frataxin in iron-sulfur cluster assembly. Hum Mol Genet 2002;11:2635–2643. [PubMed: 12354789]
10. Stehling O, Elsasser HP, Bruckel B, Muhlenhoff U, Lill R. Iron-sulfur protein maturation in human cells: Evidence for a function of frataxin. Hum Mol Genet 2004;13:3007–3015. [PubMed: 15509595]
11. Yoon T, Cowan JA. Iron-sulfur cluster biosynthesis. Characterization of frataxin as an iron donor for assembly of [2Fe-2S] clusters in ISU-type proteins. J Am Chem Soc 2003;125:6078–6084. [PubMed: 12785837]
12. Schilke B, Voisine C, Beinert H, Craig E. Evidence for a conserved system for iron metabolism in the mitochondria of *Saccharomydes cervisiae*. Proc Natl Acad Sci USA 1999;96:10206–10211. [PubMed: 10468587]
13. Garland SA, Hoff K, Vickery LE, Culotta VC. *Saccharomyces cerevisiae* ISU1 and ISU2: Members of a well-conserved gene family for iron-sulfur cluster assembly. J Mol Biol 1999;294:897–907. [PubMed: 10588895]
14. Adam AC, Bornhovd C, Prokisch H, Neupert W, Hell K. The Nfs1 interacting protein Isd11 has an essential role in Fe/S cluster biogenesis in mitochondria. EMBO J 2006;25:174–183. [PubMed: 16341090]

15. Wiedemann N, Urzica E, Guiard B, Muller H, Lohaus C, Meyer HE, Ryan MT, Meisinger C, Muhlenhoff U, Lill R, Pfanner N. Essential role of Isd11 in mitochondrial iron-sulfur cluster synthesis on Isu scaffold proteins. EMBO J 2006;25:184–195. [PubMed: 16341089]
16. Adamec J, Rusnak F, Owen WG, Naylor S, Benson LM, Gacy AM, Isaya G. Iron-dependent self-assembly of recombinant yeast frataxin: Implications for Friedreich ataxia. Am J Hum Genet 2000;67:549–562. [PubMed: 10930361]
17. Adinolfi S, Trifuoggi M, Politou AS, Martin S, Pastore A. A structural approach to understanding the iron-binding properties of phylogenetically different frataxins. Hum Mol Genet 2002;11:1865–1877. [PubMed: 12140189]
18. Bou-Abdallah F, Adinolfi S, Pastore A, Laue TM, Dennis Chasteen N. Iron binding and oxidation kinetics in frataxin CyaY of *Escherichia coli*. J Mol Biol 2004;341:605–615. [PubMed: 15276847]
19. Cavadini P, O'Neill HA, Benada O, Isaya G. Assembly and iron-binding properties of human frataxin, the protein deficient in Friedreich ataxia. Hum Mol Genet 2002;11:217–227. [PubMed: 11823441]
20. Cook JD, Bencze KZ, Jankovic AD, Crater AK, Busch CN, Bradley PB, Stemmler AJ, Spaller MR, Stemmler TL. Monomeric yeast frataxin is an iron-binding protein. Biochemistry 2006;45:7767–7777. [PubMed: 16784228]
21. He Y, Alam SL, Proteasa SV, Zhang Y, Lesuisse E, Dancis A, Stemmler TL. Yeast frataxin solution structure, iron binding, and ferrochelatase interaction. Biochemistry 2004;43:16254–16262. [PubMed: 15610019]
22. Yoon T, Cowan JA. Frataxin-mediated iron delivery to ferrochelatase in the final step of heme biosynthesis. J Biol Chem 2004;279:25943–25946. [PubMed: 15123683]
23. Gerber J, Muhlenhoff U, Lill R. An interaction between frataxin and Isu1/Nfs1 that is crucial for Fe/S cluster synthesis on Isu1. EMBO Rep 2003;4:906–911. [PubMed: 12947415]
24. Muhlenhoff U, Gerber J, Richhardt N, Lill R. Components involved in assembly and dislocation of iron-sulfur clusters on the scaffold protein Isu1p. EMBO J 2003;22:4815–4825. [PubMed: 12970193]
25. Canizares J, Blanca JM, Navarro JA, Monros E, Palau F, Molto MD. dfh is a *Drosophila* homolog of the Friedreich's ataxia disease gene. Gene 2000;256:35–42. [PubMed: 11054533]
26. Anderson PR, Kirby K, Hilliker AJ, Phillips JP. RNAi-mediated suppression of the mitochondrial iron chaperone, frataxin, in *Drosophila*. Hum Mol Genet 2005;14:3397–3405. [PubMed: 16203742]
27. Llorens JV, Navarro JA, Martinez-Sebastian MJ, Baylies MK, Schneuwly S, Botella JA, Molto MD. Causative role of oxidative stress in a *Drosophila* model of Friedreich ataxia. FASEB J 2007;21:333–344. [PubMed: 17167074]
28. Runko AP, Griswold AJ, Min KT. Overexpression of frataxin in the mitochondria increases resistance to oxidative stress and extends lifespan in *Drosophila*. FEBS Lett 2008:715–719. [PubMed: 18258192]
29. Anderson PR, Kirby K, Orr WC, Hilliker AJ, Phillips JP. Hydrogen peroxide scavenging rescues frataxin deficiency in a *Drosophila* model of Friedreich's ataxia. Proc Natl Acad Sci USA 2008;105:611–616. [PubMed: 18184803]
30. Unciuleac MC, Chandramouli K, Naik S, Mayer S, Huynh BH, Johnson MK, Dean DR. In vitro activation of apo-aconitase using a [4Fe-4S] cluster-loaded form of the IscU [Fe-S] cluster scaffolding protein. Biochemistry 2007;46:6812–6821. [PubMed: 17506526]
31. Wu SP, Wu G, Surerus KK, Cowan JA. Iron-sulfur cluster biosynthesis. Kinetic analysis of [2Fe-2S] cluster transfer from holo ISU to apo Fd: Role of redox chemistry and a conserved aspartate. Biochemistry 2002;41:8876–8885. [PubMed: 12102630]
32. Studier FW. Protein production by auto-induction in high density shaking cultures. Protein Expression Purif 2005;41:207–234.
33. van Stokkum IH, Spoelder HJ, Bloemendal M, van Grondelle R, Groen FC. Estimation of protein secondary structure and error analysis from circular dichroism spectra. Anal Biochem 1990;191:110–118. [PubMed: 2077933]
34. Hinton A, Gatti DL, Ackerman SH. The molecular chaperone, Atp12p, from *Homo sapiens*. In vitro studies with purified wild type and mutant (E240K) proteins. J Biol Chem 2004;279:9016–9022. [PubMed: 14701807]

35. Halliwell B, Gutteridge JM. Formation of thiobarbituric-acid-reactive substance from deoxyribose in the presence of iron salts: The role of superoxide and hydroxyl radicals. FEBS Lett 1981;128:347–352. [PubMed: 6266877]
36. Park S, Gakh O, Mooney SM, Isaya G. The ferroxidase activity of yeast frataxin. J Biol Chem 2002;277:38589–38595. [PubMed: 12149269]
37. Rehr JJ, Ankudinov AL. Progress and challenges in the theory and interpretation of X-ray spectra. J Synchrotron Radiat 2001;8:61–65. [PubMed: 11512868]
38. George, GN.; George, SJ.; Pickering, IJ. EXAF-SPAK. 2001. http://www-ssrl.slac.stanford.edu/~george/exafspak/exafs.htm
39. Layer G, Ollagnier de Choudens S, Sanakis Y, Fontecave M. Iron-sulfur cluster biosynthesis: Characterization of *Escherichia coli* cyay as an iron donor for the assembly of [2Fe-2S] clusters in the scaffold ISCU. J Biol Chem. 2006(in press)
40. Bencze KZ, Kondapalli KC, Cook JD, McMahon S, Millan-Pacheco C, Pastor N, Stemmler TL. The structure and function of frataxin. Crit Rev Biochem Mol Biol 2006;41:269–291. [PubMed: 16911956]
41. Adinolfi S, Nair M, Politou A, Bayer E, Martin S, Temussi P, Pastore A. The Factors Governing the Thermal Stability of Frataxin Orthologues: How To Increase a Protein's Stability. Biochemistry 2004;43:6511–6518. [PubMed: 15157084]
42. Correia AR, Adinolfi S, Pastore A, Gomes CM. Conformational stability of human frataxin and effect of Friedreich's ataxia-related mutations on protein folding. Biochem J 2006;398:605–611. [PubMed: 16787388]
43. Myers JK, Pace CN, Scholtz JM. Denaturant m values and heat capacity changes: Relation to changes in accessible surface areas of protein unfolding. Protein Sci 1995;4:2138–2148. [PubMed: 8535251]
44. Cambridge Crystallographic Data Centre. ConQuest. Vol. 1.5 . Cambridge, U.K.: 2002. Cambridge Structural Database.
45. Dailey HA, Finnegan MG, Johnson MK. Human ferrochelatase is an iron-sulfur protein. Biochemistry 1994;33:403–407. [PubMed: 8286370]
46. Yuvaniyama P, Agar JN, Cash VL, Johnson MK, Dean DR. NifS-directed assembly of a transient [2Fe-2S] cluster within the NifU protein. Proc Natl Acad Sci USA 2000;97:599–604. [PubMed: 10639125]
47. Nair M, Adinolfi S, Pastore C, Kelly G, Temussi P, Pastore A. Solution structure of the bacterial frataxin ortholog, CyaY: Mapping the iron binding sites. Structure 2004;12:2037–2048. [PubMed: 15530368]
48. Park S, Gakh O, O'Neill HA, Mangravita A, Nichol H, Ferreira GC, Isaya G. Yeast frataxin sequentially chaperones and stores iron by coupling protein assembly with iron oxidation. J Biol Chem 2003;278:31340–31351. [PubMed: 12732649]
49. Gakh O, Adamec J, Gacy AM, Twesten RD, Owen WG, Isaya G. Physical evidence that yeast frataxin is an iron storage protein. Biochemistry 2002;41:6798–6804. [PubMed: 12022884]
50. Gakh O, Park S, Liu G, Macomber L, Imlay JA, Ferreira GC, Isaya G. Mitochondrial iron detoxification is a primary function of frataxin that limits oxidative damage and preserves cell longevity. Hum Mol Genet 2006;15:467–479. [PubMed: 16371422]
51. Aloria K, Schilke B, Andrew A, Craig EA. Iron-induced oligomerization of yeast frataxin homologue Yfh1 is dispensable in vivo. EMBO Rep 2004;5:1096–1101. [PubMed: 15472712]
52. O'Neill HA, Gakh O, Park S, Cui J, Mooney SM, Sampson M, Ferreira GC, Isaya G. Assembly of human frataxin is a mechanism for detoxifying redox-active iron. Biochemistry 2005;44:537–545. [PubMed: 15641778]
53. Beneze KZ, Yoon T, Millan-Pacheco C, Bradley PB, Pastor N, Cowan JA, Stemmler TL. Human frataxin: iron and ferrochelatase binding surface. Chem Commun 2007;18:1798–1800.
54. Westre TE, Kennepohl P, DeWitt JG, Hedman B, Hodgson KO, Solomon EI. A Multiplet Analysis of the Fe K-Edge 1s → 3d Pre-Edge Features of Iron Complexes. J Am Chem Soc 1997;119:6297–6314.
55. Randall CR, Shu L, Chiou YM, Hagen KS, Ito M, Kitajima N, Lachicotte RJ, Zang Y Jr. X-ray absorption pre-edge studies of high-spin iron(II) compounds. Inorg Chem 1995;34:1036–1039.

56. Bencze, KZ.; Kondapalli, KC.; Stemmler, TL. X-Ray Absorption Spectroscopy. In: Scott, RA.; Lukehart, CM., editors. Applications of Physical Methods in Inorganic and Bioinorganic Chemistry: Handbook, Encyclopedia of Inorganic Chemistry. Vol. 2. John Wiley & Sons, Ltd.; Chichester, U.K.: 2007. p. 513-528.

57. Radisky DC, Babcock MC, Kaplan J. The Yeast Frataxin Homologue Mediates Mitochondrial Iron Efflux: Evidence for a mitochondrial iron cycle. J Biol Chem 1999;274:4497–4499. [PubMed: 9988680]

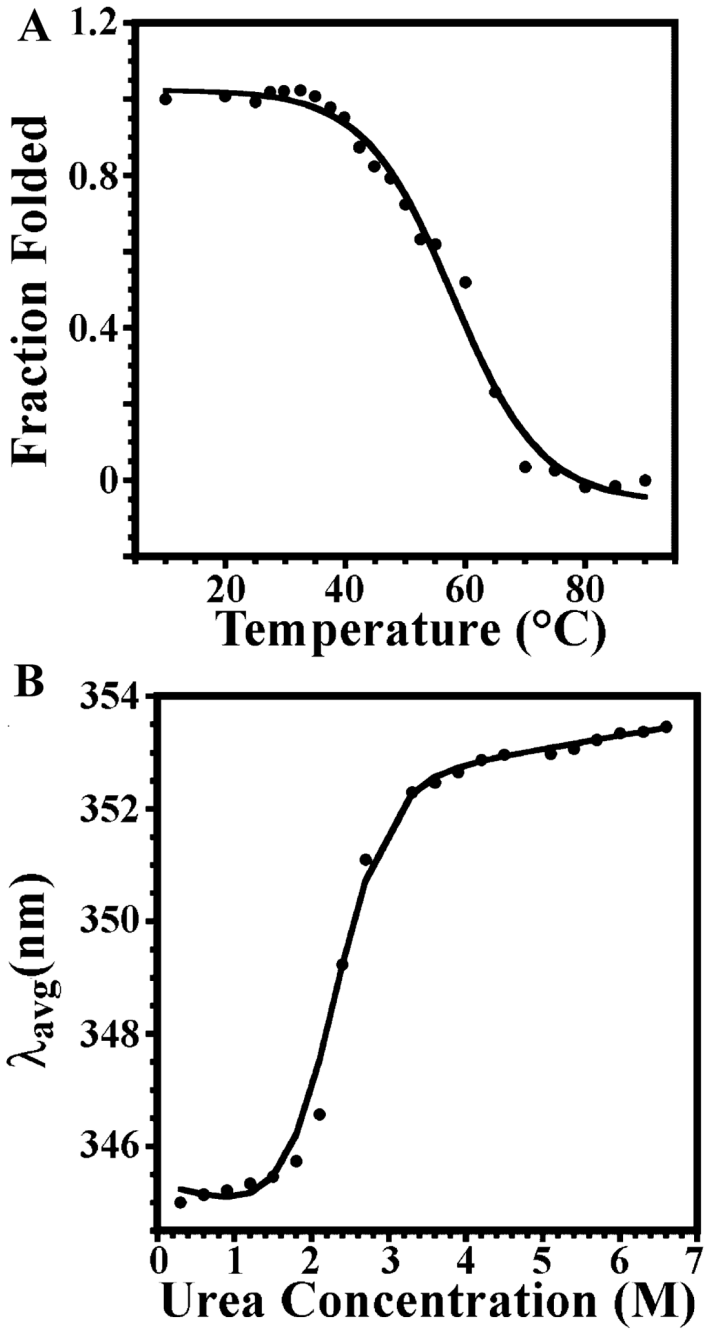

Figure 1.

Representative thermal (A) and chemical (B) denaturation profiles for apo-Dfh. In both spectra, dots represent raw data while the line represents the spectral simulation. The thermal denaturation curve for Dfh was determined by measuring changes in molar ellipticity at 208 nm from the protein's CD spectra taken at multiple temperatures. The urea denaturation curve for Dfh followed a red shift in fluorescence; spectral simulation from reproducible data sets provided the following stability parameters: $[\text{urea}]_{50\%} = 2.37 \pm 0.23$ M, $\Delta G^{H2O} = 7.44 \pm 0.47$ kcal/mol, and $m = 3.13 \pm 0.20$ kcal mol^{-1} M^{-1}.

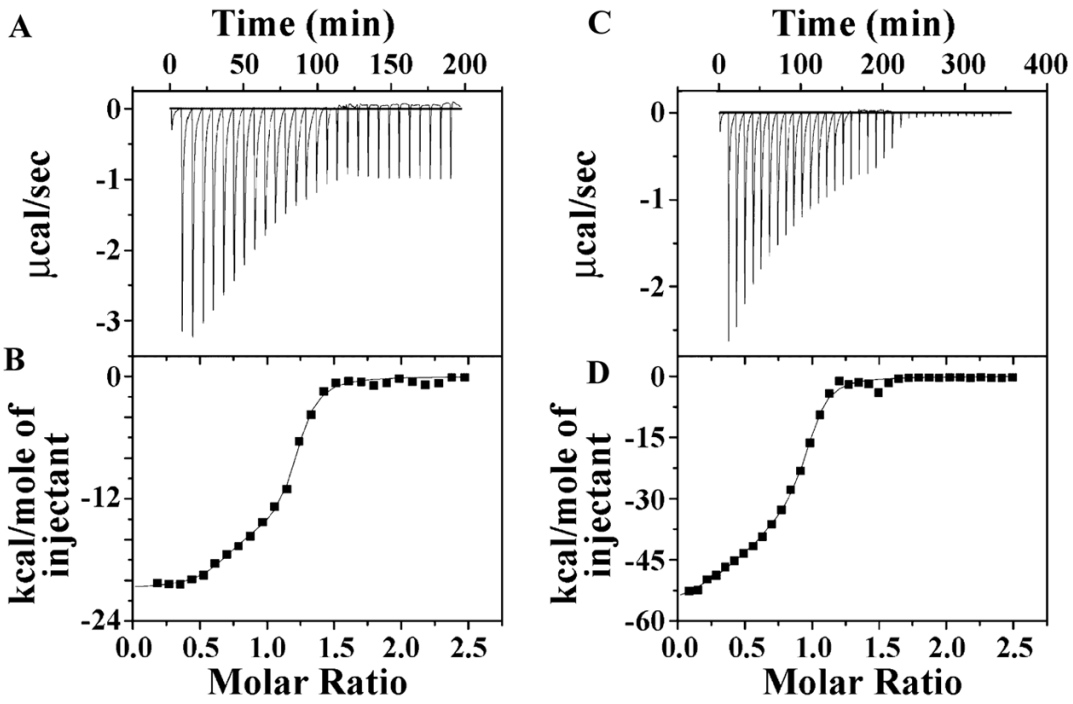

Figure 2.

Raw isothermal titration calorimetry data and binding isotherm data for ferrous iron binding to Dfh (A and B, respectively) and holo-Dfh binding to Isu (C and D, respectively). Gray lines in panels A and C show baselines for the raw ITC data. Gray lines in panels B and D show simulated fits to binding isotherm data. Data were collected anaerobically at 30 °C in 20 mM HEPES (pH 7.0) and 10 mM $MgSO_4$ for ferrous iron binding to apo-Dfh and in 20 mM HEPES (pH 7.5) and 150 mM NaCl for holo-Dfh binding to Isu.

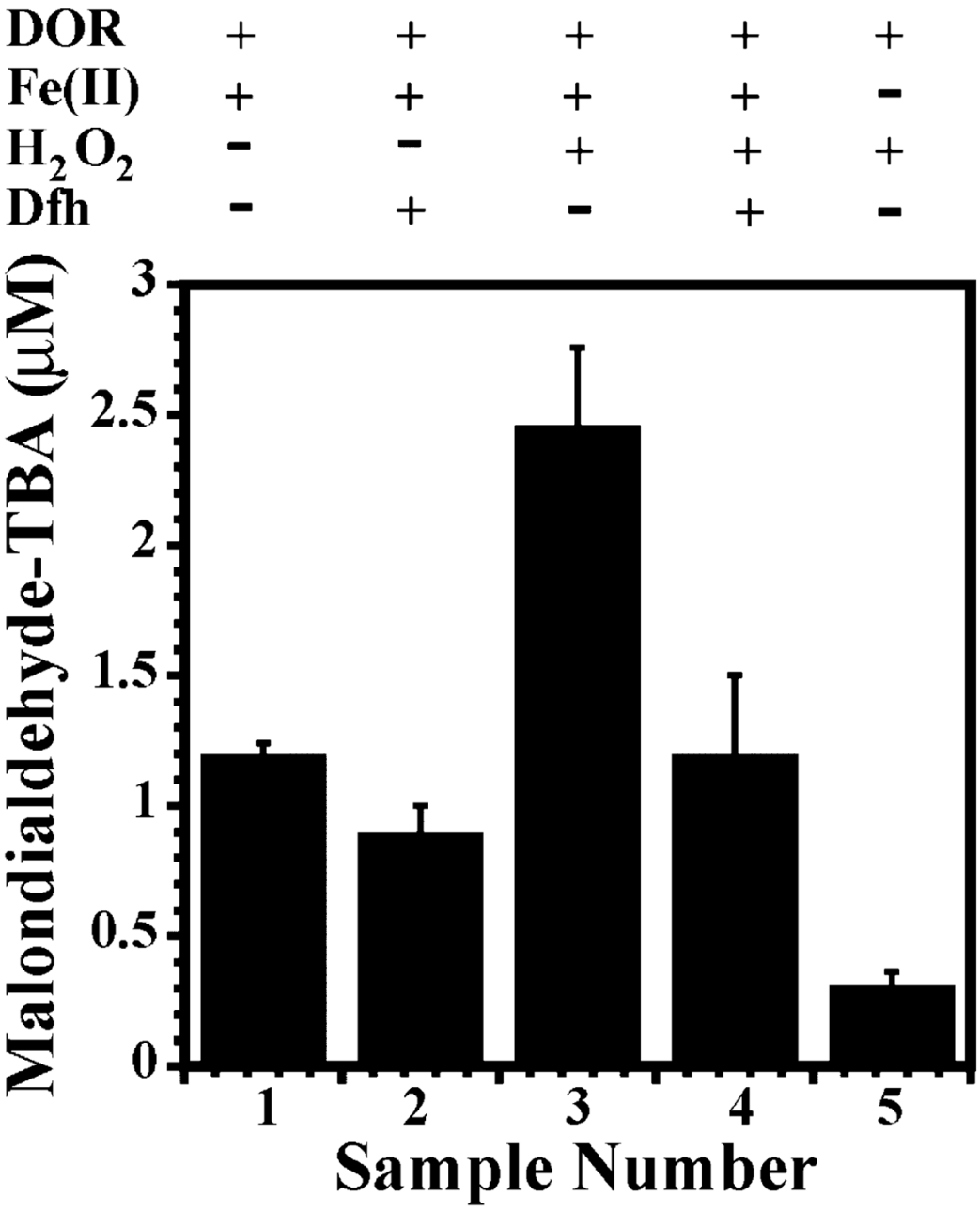

Figure 3.

Oxidative degradation assay. Reaction mixtures were incubated in the presence or absence of Dfh [in 20 mM HEPES (pH 7) and 10 mM $MgSO_4$] to test the ability of Dfh to attenuate oxidative degradation of 2-deoxyribose sugars to produce malondialdehyde.

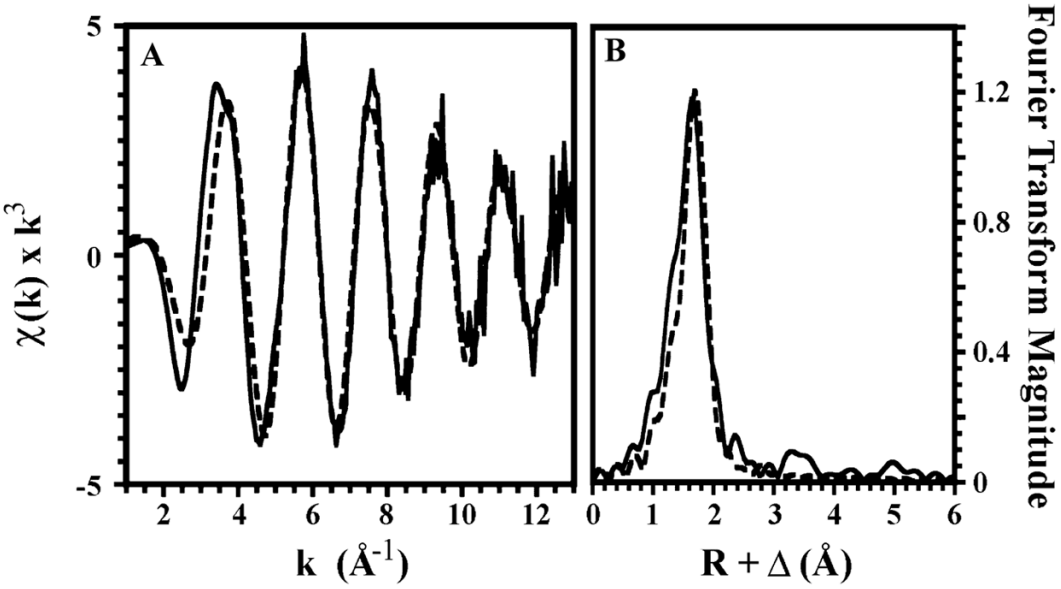

Figure 4.

EXAFS and Fourier transforms of iron-loaded Dfh. EXAFS spectra in black for Dfh with one iron bound (A) with the corresponding Fourier transform (B). Simulations for EXAFS and FT data are shown with a dashed line.

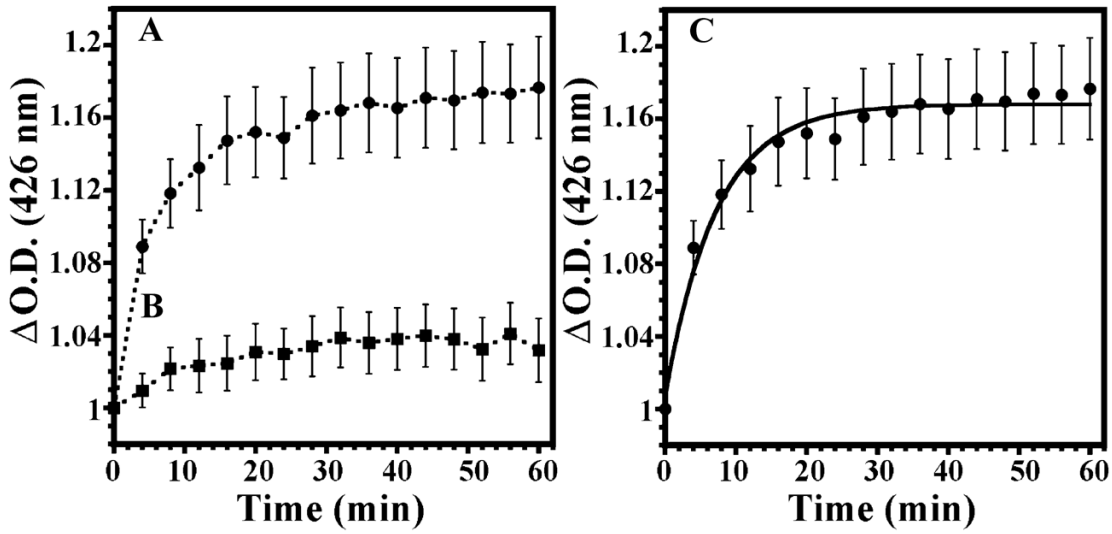

Figure 5.

Time dependence for formation of the Fe–S cluster on ISU. The solution contained 100 μM Isu, 4.3 mM DTT, and 2.4 mM Na_2S in 20 mM HEPES buffer (pH 7.5), with 150 mM NaCl to which Fe(II) was added as holofrataxin (● in part A) or directly (■ in part B) to a final concentration of 100 μM. Reaction progress was monitored at 426 nm. (C) Time dependence data (●) from panel A fit with a rate equation for a first-order process (simulation as a solid line). Error bars represent the average values at each time point from the three independent reproducible experiments that were conducted.

Table 1

Summary of the Best EXAFS Fitting Results for Iron-Loaded Dfh[a]

fit	no. of shells[b]	atom[c]	*R* (Å)[d]	CN[e]	σ^2 [f]	*F′* [g]
1	**1**	**O/N**	**2.13**	**4.50**	**5.23**	**0.53**
2	1	S	2.29	1.00	2.54	3.06
3	2	O/N	2.09	2.00	1.00	0.50
		O/N	2.19	2.00	2.16	
4	2	O/N	2.17	4.00	5.52	0.80
		S	2.23	1.00	3.50	

[a] Data were fit over a *k* range of 1–13 $Å^{-1}$. Best fit parameters are in bold. The resolvable bond length resolution is 0.13 Å.

[b] Independent nearest-neighbor metal–ligand scattering environments.

[c] Scattering atoms.

[d] Metal–ligand bond length.

[e] Metal–ligand coordination number.

[f] Debye–Waller factor in $Å^2 \times 10^3$.

[g] Number of degrees of freedom weighted mean square deviation between data and fit.